Review of Scientific Instruments

A novel experimental apparatus for investigating bubbly flows in a slot geometry

Cite as: Rev. Sci. Instrum. **91**, 045110 (2020); https://doi.org/10.1063/1.5126775
Submitted: 05 September 2019 . Accepted: 24 March 2020 . Published Online: 14 April 2020

Antonio Capponi, Andrew C. Crosby, Stephen Lishman, and Edward W. Llewellin

Review of Scientific Instruments ARTICLE scitation.org/journal/rsi

A novel experimental apparatus for investigating bubbly flows in a slot geometry

Cite as: Rev. Sci. Instrum. 91, 045110 (2020); doi: 10.1063/1.5126775
Submitted: 5 September 2019 • Accepted: 24 March 2020 •
Published Online: 14 April 2020

Antonio Capponi,[1,2,a)] Andrew C. Crosby,[3] Stephen Lishman,[3] and Edward W. Llewellin[1]

AFFILIATIONS

[1] Department of Earth Sciences, Durham University, Durham DH1 3LE, United Kingdom
[2] Lancaster Environment Centre, Lancaster University, Lancaster LA1 4YQ, United Kingdom
[3] Mechanical Engineering Services, Department of Physics, Durham University, Durham DH1 3LE, United Kingdom

[a)] **Author to whom correspondence should be addressed:** a.capponi2@lancaster.ac.uk

ABSTRACT

Bubbly flows occur in a wide variety of industrial and environmental settings. While there is a broad literature that describes bubbly flow behavior in pipes and channels, flow in a high aspect ratio slot has received little attention. We describe the design and construction of a new experimental apparatus to investigate the processes associated with bubbly flows in a slot geometry. The apparatus is designed to perform scaled analog experiments to investigate the flow of bubbly magma through the sub-volcanic plumbing system, but it is sufficiently flexible to address many other flow scenarios. The main bubble column, which can be inclined up to 30° from the vertical, comprises a glass-walled slot 3 m wide and 2 m tall, with 3 cm gap width. A modular and flexible gas injection system allows the number, spacing, and diameter of the gas emission points to be varied, as well as gas injection flux, and a pumped recirculation system allows the concurrent liquid flow rate to be controlled and varied. A dedicated data acquisition system synchronizes high-speed videography with temperature and pressure data from different points in the apparatus. Preliminary data are presented to demonstrate the operation of the apparatus and to illustrate the types of fluid dynamic information that can be captured.

I. INTRODUCTION

Bubbly flows are common in both industrial settings (e.g., food and beverage manufacture, nuclear reactors, hydrocarbon recovery, mineral extraction, and waste processing) and environmental settings (e.g., volcanic eruptions, lava flows, geysers, high-energy rivers, and breaking ocean waves). While the flow of bubbly liquids in channels and pipes is well investigated, flow in slots or high-aspect ratio ducts has received little attention. This work describes the design, construction, and operation of a novel experimental apparatus for the quantitative investigation and characterization of bubbly flow in a slot geometry. The development of the apparatus was motivated by a desire to investigate the flow of bubbly magma during basaltic fissure eruption—the most common type of volcanic eruption on Earth (Houghton and Gonnermann, 2008). Nonetheless, the apparatus is sufficiently flexible that it can also be used to investigate bubbly flows of industrial relevance, such as the flow of petroleum oil, below its bubble-point pressure, along cracks and annular wells.

Basaltic magma moves through the Earth's crust along cracks, called "dykes" (Lister and Kerr, 1991; Rubin, 1995). When a dyke intersects the Earth's surface, it produces a fissure eruption, which is characteristic of many of the most active basaltic volcanoes, such as Kīlauea (Hawai'i), Piton de la Fournaise (Réunion Island, France), Erta'Ale (Ethiopia), Nyiragongo (Democratic Republic of Congo), Etna (Italy), and most Icelandic volcanoes. Over a period of days to weeks, fissure eruptions tend to localize to form a single, roughly circular eruptive vent (or a small number of such vents) and, for longer-lived eruptions, the shallow part of the plumbing system may evolve to become pipe-like (Bruce and Huppert, 1989). A pipe geometry is much simpler to model in the laboratory than a slot geometry; consequently, previous experimental work in multiphase volcanological fluid dynamics has focused almost exclusively on flow in a pipe (Seyfried and Freundt, 2000; Lane *et al.*, 2001;

James *et al.*, 2004, 2008; Pioli *et al.*, 2012; Del Bello *et al.*, 2015; and Capponi *et al.*, 2016, 2017), and we are aware of only one experimental study that adopts a slot geometry (Pioli *et al.*, 2017). As a consequence, fluid dynamics within a dyke is poorly understood, despite its obvious importance in the transport and eruption of basaltic magma.

Magma is a complex multiphase material, comprising a continuous silicate melt (liquid) that suspends bubbles (gas) and crystals (solid) in variable proportions. Silicate melt of basaltic composition typically has a viscosity of $10–10^4$ Pa s at eruption temperature (Shaw, 1969; Vergniolle, 1996, 1998). As a consequence of its relatively low viscosity compared with other melt compositions, the suspended bubbles—which form when volatile species dissolved in the melt at depth come out of solution as the magma rises and decompresses—can rise through the melt with an appreciable slip velocity (Parfitt, 2004). The relative proportion and velocity of the melt and gas phases is thought to be the principal control on the eruption style of basaltic volcanoes [Figs. 1(a)–1(d)]. The experimental evidence that supports and informs this paradigm is, however, derived mainly from experiments in pipes [Figs. 1(e)–1(h)]. The experimental apparatus described here is intended to address this weakness and provide an evidence base for understanding the eruption behavior in terms of flow processes that occur when bubbly magma is transported to the surface along a dyke-like conduit. This geometry allows lateral flow patterns to develop (Pioli *et al.*, 2017) and the additional degree of freedom is likely to modify the fluid dynamic phenomena observed in pipe-flow, and to introduce additional phenomena that have not previously been described.

The chief design considerations for the experimental apparatus are: (1) safety and budget, which place constraints on the size and design of the apparatus, and on standard operating procedures, (2) faithful encapsulation of the behavior of the natural system, which includes effective scaling such that dynamic similarity with basaltic fissure eruptions can be achieved across a broad range of conditions, and flexibility to vary the boundary conditions and tilt angle of the

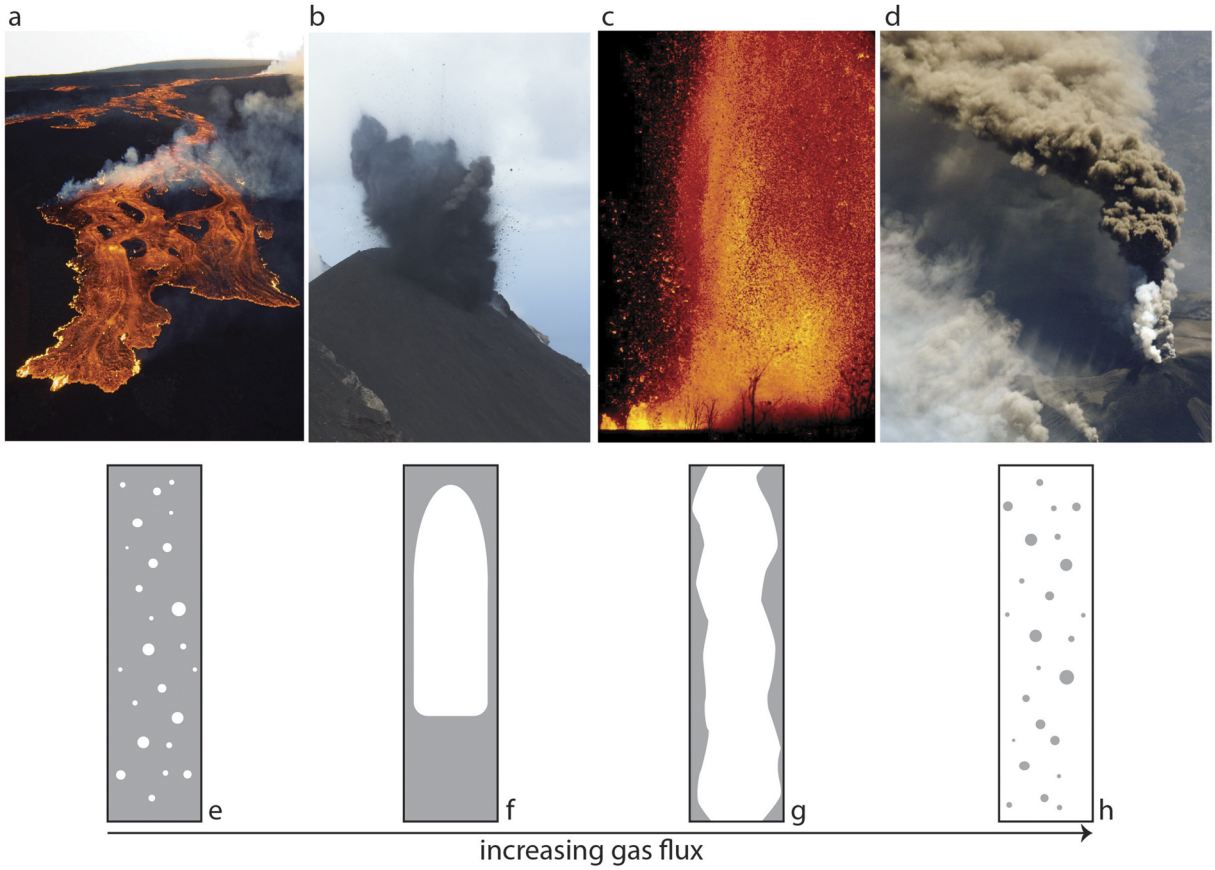

FIG. 1. Main eruptive styles at basaltic volcanoes: (a) lava flow produced by erupting vents on Mauna Loa's northeast rift zone near Pu'u 'Ula'ula (Red Hill) on March 25, 1984 (Courtesy of USGS website, https://www.usgs.gov/media/images/erupting-vents-mauna-loas-northerz-near-pu-u-ula-ula-red-hill). (b) Typical ash-rich and ballistic-rich Strombolian eruption at Stromboli (Courtesy of A. Capponi). (c) High lava fountain during the fourth episode of fountaining of Mauna Ulu eruption on June 25, 1969 (Courtesy of USGS website, https://volcanoes.usgs.gov/vsc/images/image_mngr/5000-5099/img5072.jpg). (d) View from the International Space Station of the Etna eruptive ash column on October 30, 2002 (Courtesy of NASA, https://eoimages.gsfc.nasa.gov/images/imagerecords/2000/2923/etna2_ISS2002303_lrg.jpg). Two-phase flow regimes in vertical cylindrical conduit (after Vergniolle and Jaupart, 1986; Pioli *et al.*, 2012): (e) bubbly flow, (f) slug flow, (g) annular flow, and (h) dispersed flow.

main flow, and (3) ease of operation, which includes accurate and straightforward control of input experimental variables and collection of output data. These considerations are, to some extent, in competition, such that the final design represents the best compromise that we could achieve. This article describes the components, features, and operation of the apparatus in the context of the design considerations that informed them. Our goal is to allow others to replicate and improve upon our design.

II. VOLCANOLOGICAL BACKGROUND

Dykes are magma-filled slots with width W typically ranging from a few tens of centimeters to a few meters, and length L typically ranging from a few tens of meters to many tens of kilometers (Rubin, 1995; Parcheta *et al.*, 2012; and Gonnermann and Taisne, 2015). The slots are formed by brittle cracking of crustal rock as magma propagates from the crustal reservoir toward the surface. The walls are, therefore, irregular and are modified by syn-eruptive dynamic erosion, local wall collapses, and conduit narrowing due to cooling and solidification of magma along the walls (Parcheta *et al.*, 2015). Dyke orientation is controlled regionally by tectonic structures and stresses (Chouet *et al.*, 2010) and locally by the structural properties of the volcanic edifice. Thus, although dykes usually propagate through the deep crust as sub-vertical and steep cracks, in the shallow crust, they can also propagate laterally as inclined sheets, with inclination depending on the shape and load of the volcanic edifice, remote tectonic forces, overpressure within the dyke, and crustal heterogeneities (Pinel and Jaupart, 2000; Kervyn *et al.*, 2009; and Tibaldi *et al.*, 2014). Basaltic magmas that fill the dykes typically have a viscosity in the range of $10–10^4$ Pa s and density in the range of 800–2600 kg/m^3, controlled mainly by the bubble content (Shaw, 1969; Murase and McBirney, 1973; Métrich *et al.*, 2001; and Gurioli *et al.*, 2014). Surface tension values, as measured by Murase and McBirney (1973) for several basaltic liquids, are in the range of 0.07–0.4 N/m. For a typical basaltic magma, a surface tension value of 0.08 N/m is generally assumed (Pioli *et al.*, 2017).

When a propagating dyke intersects the ground surface, it forms a fissure eruption (Reynolds *et al.*, 2017) with magma flux driven by the pressure difference, above magmastatic, between the crustal reservoir and the surface (Rubin, 1995; Valentine and Gregg, 2008). During this type of eruption, magma usually erupts simultaneously as lava fountains from several emission points along the fissure length, spanning for tens of meters up to several kilometers (Parcheta *et al.*, 2015). The fountains can have heights from tens up to hundreds of meters. As the eruption evolves, magma emission focuses on fewer vents along the fissure until either the eruption ends, or it localizes to a single point source (Thorarinsson *et al.*, 1973; Swanson *et al.*, 1979; and Bruce and Huppert, 1989). To date, the mechanisms controlling the temporal and spatial evolution of fissure eruptions are still poorly understood, but thermo-rheological behavior of the magma (Bruce and Huppert, 1989) and flow organization in the dyke (Pioli *et al.*, 2017) are thought to be important controlling processes. Figure 2 shows an example of a recent fissure eruption, along with a conceptual sketch showing some of the inferred subsurface flow processes. Fountain height is the main observable parameter used to constrain eruptive parameters, such as gas content, volume fluxes, lava re-entrainment, and gas bubble coalescence (Parfitt *et al.*, 1995; Wilson *et al.*, 1995). However, the surface activity can be influenced by the presence of ponded lava in the vent region, and by the formation of spatter ramparts, constructed from agglutinated spatter (Parcheta *et al.*, 2012; Jones *et al.*, 2017). The effects of ponding on fountain dynamics are still poorly understood.

The eruption style is strongly influenced by the organization of the gas phase in the magma (Valentine and Gregg, 2008). The relatively low viscosity of basaltic melt allows bubbles to rise through it with an appreciable slip velocity, supporting bubble coalescence, and the formation of large gas "slugs," driving strombolian activity (Parfitt, 2004; Vergniolle and Gaudemer, 2015). Crystallization also plays a role through its effect on the magma rheology. Abundant microlite growth increases the magma viscosity, which may lead to an increase in small bubbles that are unable to rise faster than the melt and to coalesce, while at the same time favoring shallow degassing by producing bubble nucleation sites (Valentine *et al.*, 2005). Crystals may also introduce shear thinning behavior and non-Newtonian phenomena (Mueller *et al.*, 2011). Furthermore, the

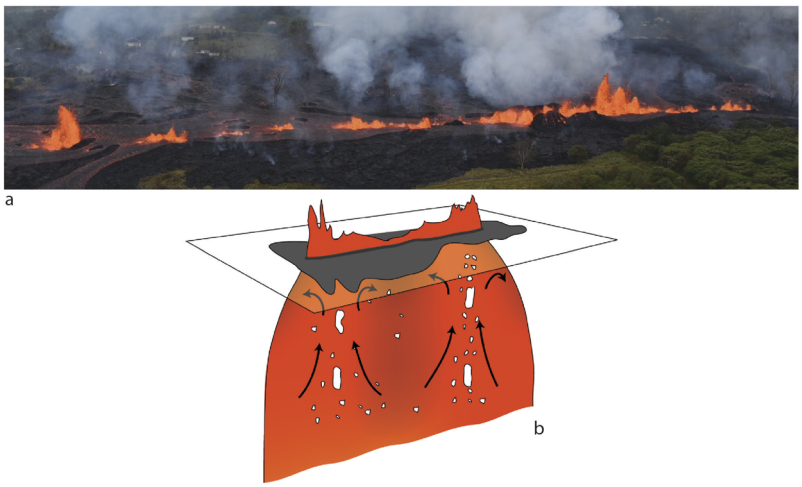

FIG. 2. Lava fountains from Fissure 20 in Kīlauea Volcano's lower East Rift Zone, May 19, 2018 [(a); Courtesy of USGS HVO, https://volcanoes.usgs.gov/observatories/hvo/multimedia_uploads/multimediaFile-2059.jpg] and (b) conceptual sketch of the expected flow pattern in a fissure geometry.

downwelling drain-back of a denser and degassed lava within the fissure, together with the upwelling flow of a fresh hotter magma, may initiate a bidirectional exchange flow within the fissure. Such bidirectional flows have been investigated quite extensively in the case of cylindrical geometry (Stevenson and Blake, 1998; Palma *et al.*, 2011; and Beckett *et al.*, 2014) but the organization of upwelling and downwelling components in a fissure geometry, and the impact on the resulting surface activity, is still poorly investigated.

III. DESIGN OF THE APPARATUS

We have designed and constructed a new experimental apparatus to investigate flow processes in a multiphase bubble–liquid flow ascending a dyke-like conduit (Fig. 3). It has dimensions of 3.2 × 3.1 × 3.2 m (length, height, width), and weighs ~7 tons, including working fluid. The apparatus is designed to be safely operated by one person (two for some operations), using low-hazard analog fluids. Dimensions and working fluids are chosen to ensure the dynamic and geometric similarity with natural magmatic systems, and the apparatus is designed to allow accurate and systematic control of relevant parameters (e.g., gas and liquid fluxes, bubble column inclination, spacing, and number of gas emission points) and to allow easy visualization and measurement of the resulting flow behavior.

The apparatus comprises three main sections: (1) a rectangular bubble column (i.e., the analog dyke) of internal dimensions 3.0 × 2.0 × 0.03 m, connected at the top and bottom to two tanks of

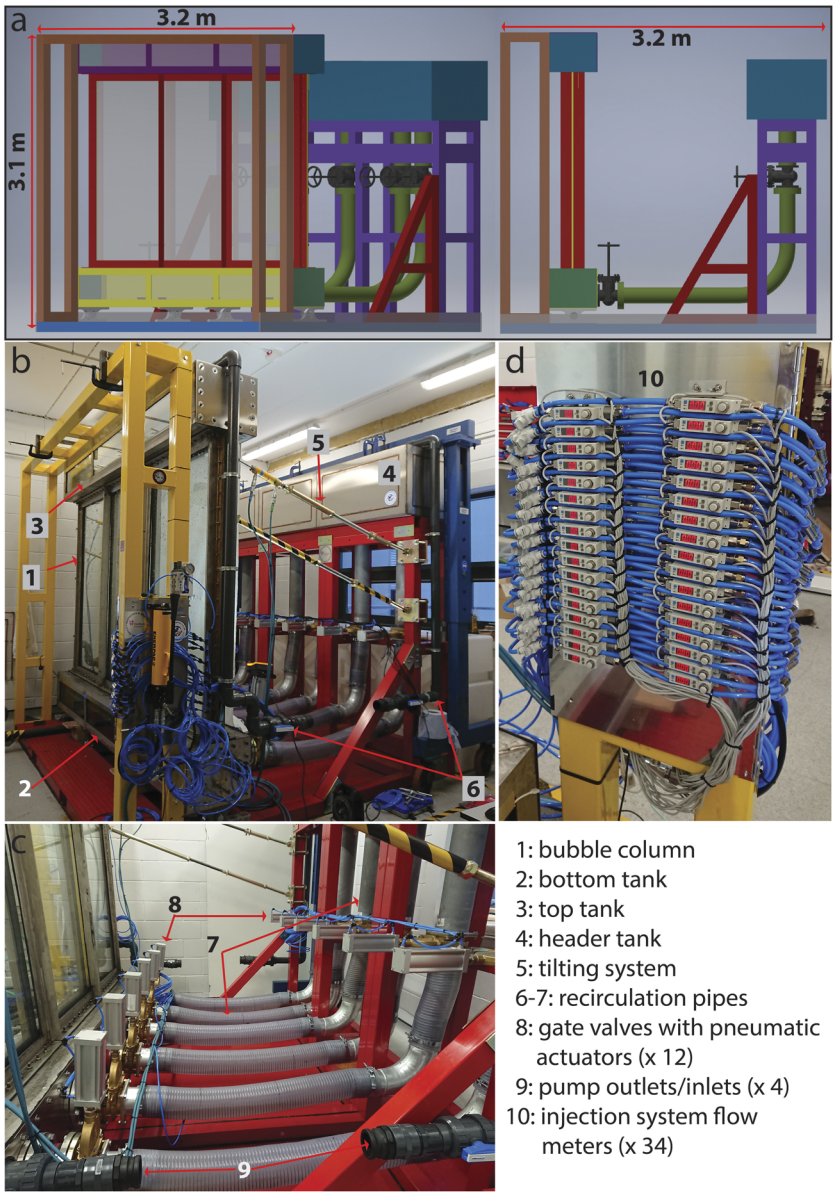

FIG. 3. (a) Technical drawing of the experimental apparatus; (b) and (c) views of the assembled apparatus; and (d) view of the control panel for the gas injection system.

dimensions 3.15 × 0.4 × 0.5 m each [Fig. 3(b)]. A tilting system allows for the main bubble column to tilt up to 30° [Fig. 3(b)]. (2) A recirculation system, to allow control of liquid fluxes [Figs. 3(b) and 3(c)], linked to (3) a rear 3.15 × 0.6 × 0.7 m header tank [Fig. 3(b)]. The entire apparatus is supported by a metal scaffolding, fixed to a 3.25 × 0.1 × 3.2 m reinforced base. A customizable bubbler unit sits in the bottom tank, giving flexible control on gas fluxes and on the number, spacing, and diameter of gas emission points.

A. Scaling

The use of analog experiments to investigate flow phenomena in volcanic conduits depends on rigorous scaling from laboratory to nature. To achieve this, the analog and natural systems must be geometrically and dynamically similar. Geometric similarity, i.e., in the ratios of length, width, and height, is required so that the influence of the boundaries on the emergent flow patterns is comparable. Dynamic similarity ensures that the ratios among the various forces acting on the flow in the natural system—arising from pressure gradients, viscosity, inertia, surface tension, and buoyancy—are matched in the experimental conditions.

Volcanic dykes typically have aspect ratios in the range of 10^{-3}–10^{-4} (Rubin, 1995; Valentine and Perry, 2006; and Gonnermann and Taisne, 2015). At the laboratory scale, this would require such a thin analog dyke that it would compromise dynamic scaling. Achieving the smallest practical aspect ratio is part of the motivation for the large size of the experimental apparatus; for our apparatus geometry, $W/L = 10^{-2}$. While this is somewhat larger than the aspect ratio of the natural system, it is small enough to ensure that the influence of the slot walls on the flow dominates that of the end walls, as in the natural system.

To achieve dynamic similarity, we must identify the dimensionless groups that best describe the physical behavior of the natural system. The range of values of these dimensionless groups should match in the analog experiments. The dimensional quantities that are most relevant to flow processes in a volcanic conduit are: liquid viscosity μ (Pa s), liquid density ρ (kg/m^3), gas–liquid surface tension σ (N/m), conduit width (experimentally expressed as hydraulic diameter) D (m), gravitational acceleration g (m/s^2), and the velocity of the ascending gas and/or liquid V (m/s). The dimensionless combinations of these parameters commonly used to describe a system are: the Eötvös number Eo; the Froude number Fr; the Reynolds number Re; and the inverse viscosity N_f (e.g., Seyfried and Freundt, 2000; James *et al.*, 2004, 2008; Llewellin *et al.*, 2012; Del Bello *et al.*, 2015; and Capponi *et al.*, 2017).

The Eötvös number represents the ratio of buoyancy and surface tension forces,

$$\mathrm{Eo} = \frac{\rho g D^2}{\sigma}. \tag{1}$$

The Reynolds number represents the ratio of inertial and viscous forces; in a high-aspect ratio slot, it is given by

$$\mathrm{Re} = \frac{2\rho D V}{\mu}. \tag{2}$$

The Froude number is a dimensionless velocity, representing the ratio of inertia and gravitational forces

$$\mathrm{Fr} = \frac{V}{\sqrt{gD}}. \tag{3}$$

The inverse viscosity is given by (Wallis, 1969)

$$N_f = \frac{\rho}{\mu}\sqrt{gD^3}. \tag{4}$$

Table I shows the expected values of dimensional and dimensionless quantities for basaltic volcanoes. The high range of Eo suggests that surface tension plays a negligible role in basaltic magmas, and hence that flow processes are mostly controlled by inertial and viscous forces; previous work on similar systems has shown that surface tension effects can be neglected for Eo $\gtrsim$ 40 (Seyfried and Freundt, 2000; Viana *et al.*, 2003; and Llewellin *et al.*, 2012). Previous experimental studies have also shown that the inverse viscosity N_f is the key scaling parameter in the high Eötvös number regime (Seyfried and Freundt, 2000; James *et al.*, 2008; and Llewellin *et al.*, 2012). The inverse viscosity can be thought of as a Reynolds number in which the velocity is replaced with the scale velocity $\sqrt{gD}$, and hence it is particularly useful as an independent (i.e., controlled) variable because it contains only material and system parameters, and includes no parameters that must be determined experimentally. The Reynolds number can be inferred based on field estimates of flow velocities (e.g., Orr *et al.*, 2015), and falls within the range of $10^{-3} < \mathrm{Re} < 10^3$, indicating that dyke flow is typically in the laminar regime, but may be turbulent during the most vigorous basaltic eruptions (Mastin *et al.*, 2004).

Magmas are three-phase systems, comprising a solid (crystal), liquid (silicate melt), and gas (bubble) phase. Pure silicate melts have Newtonian rheology, but magma with appreciable bubble and/or crystal fraction (total suspended fraction above around 50%) has increasingly non-Newtonian rheology (Mader *et al.*, 2013). For simplicity, we only consider scaling of Newtonian analog fluids in this contribution: water and golden syrup. Relevant dimensional and dimensionless quantities for the analog materials are given in Table I. The dimensions of the apparatus ensure that experiments remain in the high Eötvös number regime (Eo $\gtrsim$ 40). With the given apparatus dimensions and liquid properties, we can cover

TABLE I. Comparison of experimental parameters for water and syrup from this study, and scaling to the volcanic case.

Material	Basaltic volcanoes	Water	Syrup
Density ρ (kg/m^3)	800–2800	1000	1430
Viscosity μ (Pa s)	10–10^4	0.001	50–100[a]
Surface tension σ (N/m)	0.08	0.07	0.08[b]
Gravity g (m/s^2)	9.81	9.81	9.81
Conduit width D (m)	0.5–10	0.03	0.03
Eötvös number Eo	10^4–10^7	5×10^2	1.8×10^2
Froude number **Fr**	10^{-3}–0.34	0.34	6.4×10^{-3}
Reynolds number Re	10^{-3}–10^3	1.5×10^4	5×10^{-3}
Inverse viscosity N_f	10^{-1}–10^4	4.6×10^4	2.3×10^{-1}

[a]For a temperature range of ~15°–25 °C (Llewellin *et al.*, 2002). Note that the syrup viscosity is dependent on temperature.
[b]Llewellin *et al.*, 2002.

the full range of inverse viscosity expected in the natural system. Table II shows how our parameter space coverage compares with ranges of N_f, Eo, and Fr covered by some of the major experimental investigations in the literature.

B. The apparatus

The bubble column frame and all the tanks were constructed using 5-mm-thick panels of 316 stainless steel, also known as marine grade stainless steel, which was chosen for its strength and resistance to corrosion. The reinforced base and the main scaffolding were constructed using mild steel, either yellow-passivated or powder-coated before assembling to ensure a higher resistance to rust, corrosion, and scratches.

The main bubble column consists of two opposite frames of equal dimensions, 3.15 m in length and 2 m in height, housing two large laminated glass panels 3 × 2 m (Fig. 4). Each panel (manufactured by Romag Ltd., Leadgate Industrial Estate, Leadgate, Consett DH8 7RS) was laminated by bonding two layers of toughened glass, 15 mm and 12 mm thick, respectively. The two layers are separated by a 1.5-mm-thick SentryGlas Plus (SGP) interlayer. The choice of type of glass, the interlayer, and their thicknesses were guided by the requirement that the panels should be as thin as possible (minimizing weight and optical distortion), yet sufficiently rigid to avoid significant deformation in operation. Compared to the more common annealed glass, toughened glass is both stronger and more rigid. The more conventional polyvinyl butyral (PVB) interlayer offers an excellent protection against sudden and temporary loads; however, under long-term loads, PVB starts to creep and the glass layers behave as if they are decoupled. The SGP interlayer is characterized by a higher tear-strength and higher rigidity, and is thinner, lighter, and stiffer than PVB, allowing an efficient transfer of load between the glass layers, reducing deflection. To accommodate the glass deformation and displacement within the frame when under load, the panels were glazed using structural sealant Sikaflex®-265, which is a high-performance elastic adhesive that is both water- and chemical-resistant. To further reduce panel deformation, we added two supporting beams within each frame, at a spacing of 1 m [Figs. 4(a) and 4(c)]. According to these specifications, simulations of glass deformation, conducted by the manufacturer, give a maximum glass deflection of 4 mm when the apparatus is filled with a 2.5-m-high liquid column with a density of 1400 kg/m^3. To allow the gas–liquid mixture to flow upward, we created a 3-cm-wide gap between the two glass panels by inserting two 1.5-cm-thick layers of rubber all along the edges of the stainless-steel frames [Figs. 4(a) and 4(b)].

The bubble column is attached to the top and bottom front tanks [Fig. 4(d)] using a 1.5-cm-thick rubber gasket as a sealant. The front panel of both the top and bottom front tanks is fitted with three glass panels to permit observations.

The top tank is open to the atmosphere, and acts mainly as a collector tank for the liquid flowing upward through the bubble column. On both sides of this tank, two pipes of diameter 7.6 cm are fitted within it, with the inlets at 10 cm above the exit of the bubble column. The pipes are part of the recirculation system [Figs. 3(b) and 3(c)] and run down along both sides of the main frame, to two ball valves, in turn connected to quick-release fittings and to the inlet of

TABLE II. Comparison of experimental parameters between this study and some of the previous major experimental investigations in the literature.

References	Geometry, inclination	D (m)	μ (Pa s)	ρ (kg/m^3)	N_f[a]	Eo[a]	Fr[a]
Jaupart and Vergniolle, 1989	Cylindrical, 0°	0.044	0.009–1.2	930–1262	5–2890	365–880	0.05–0.34
Seyfried and Freundt, 2000	Cylindrical, 0°	0.014, 0.05	0.001–1.2	1000–1400	$29–3.5 \times 10^4$	27–350	0.20–0.34
James *et al.*, 2004	Cylindrical, 0°–40°	0.038	0.001–0.9	1000–1320	$3.4 \times 10^1–2.3 \times 10^4$	200–267	0.21–0.34
James *et al.*, 2006	Cylindrical, 0°	0.038, 0.08	0.001–30	1000–1340	$1.04–2.3 \times 10^4$	$200–1.2 \times 10^3$	0.01–0.34
James *et al.*, 2008	Cylindrical, 0°	0.025	0.124	862	91	179	0.32
Kobayashi *et al.*, 2010	Cylindrical, 0°	0.056	0.001–120	1000–1450	$5 \times 10^{-1}–4.1 \times 10^4$	439–637	0.004–0.34
Llewellin *et al.*, 2012	Cylindrical, 0°	0.02–0.08	0.001–40	895–1390	$3.1 \times 10^{-1}–5.9 \times 10^4$	$66–3 \times 10^3$	0.002–0.36
Pioli *et al.*, 2012	Cylindrical, 0°	0.24	0.001–280	1000–1450	$1.8–3.6 \times 10^5$	$75–1 \times 10^4$	0.018–0.34
Lane *et al.*, 2013	Cylindrical, 0°	0.025	0.162	860	65	75	0.28
Del Bello *et al.*, 2015	Cylindrical, 0°	0.025	0.001, 1	961, 1000	$12, 1.2 \times 10^4$	87, 196	0.10, 0.34
Spina *et al.*, 2016	Cylindrical, 0°	0.02	1–1000	970	$8.5 \times 10^{-3}–8.5 \times 10^0$	95	$7.3 \times 10^{-5}–8.1 \times 10^{-3}$
Capponi *et al.*, 2017	Cylindrical, 0°	0.025	0.1, 1	961, 990	12, 122	15, 196	0.10, 0.30
Pioli *et al.*, 2017	Fissure, 0°	0.06[b]	0.001–70	1000–1400	$9.2 \times 10^{-1}–4.6 \times 10^4$	$5 \times 10^2–6 \times 10^2$	0.009–0.34
This study	Fissure, 0°–30°	0.06[b]	0.001–100	910–1430	$6.5 \times 10^{-1}–4.6 \times 10^4$	$1.8 \times 10^2–5 \times 10^2$	0.006–0.34

[a]Dimensionless values calculated with Eqs. (1), (3), and (4), using liquid properties and apparatus dimensions reported in the main text.
[b]Hydraulic diameter calculated as twice the slot width.

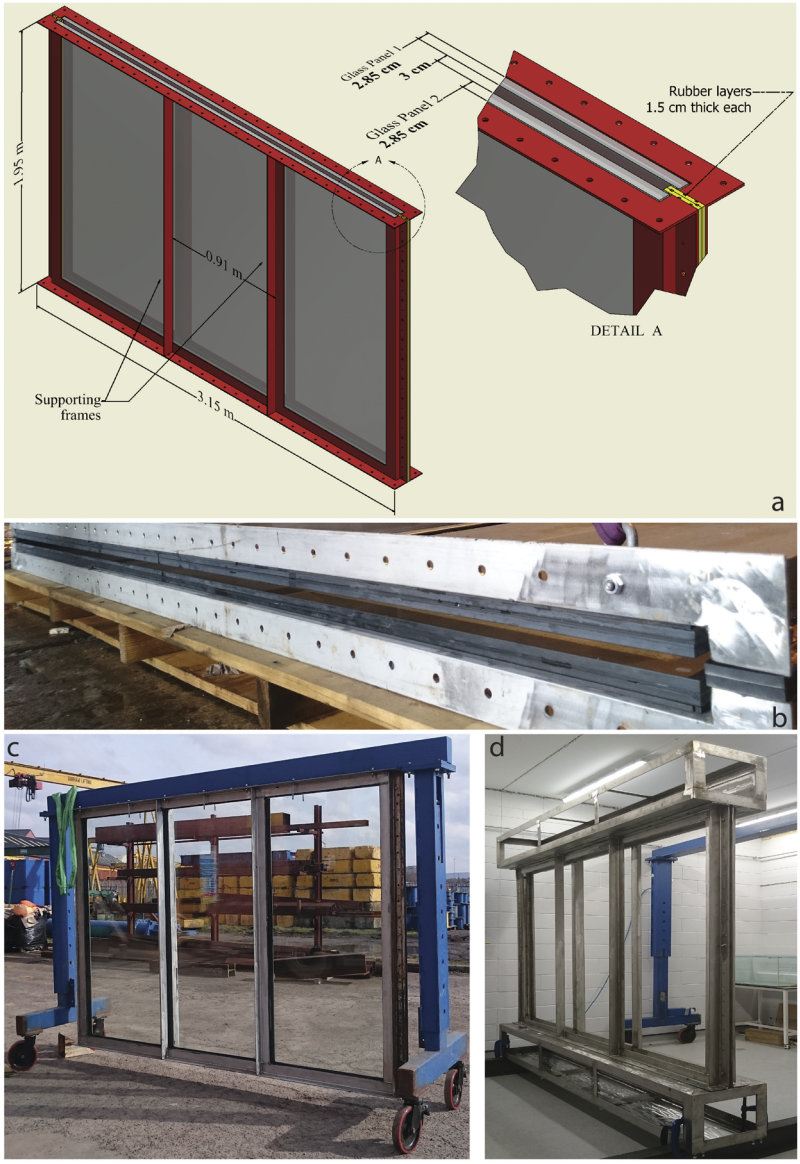

Fig. 4. (a) Technical drawing of the main bubble column. (b) The 3-cm-wide gap acting as the experimental slot, created by the rubber layers. (c) View of the bubble column just after assembly. (d) The bubble column attached between the top and bottom tanks during assembly.

a pump [Fig. 3(c)]. After being collected from the top tank, the liquid is pumped into the header tank at the rear via a similar piping system. At the bottom of the header tank, six galvanized hose tails are connected, via six gate valves of internal diameter 15.2 cm, to six pipes of equal diameter that run down to the rear panel of the bottom tank in the main section [Fig. 3(c)]. The total cross-sectional area of the pipes is bigger than the area of the fissure. Calculations of pressure drop across the pipes and across the bubble column for turbulent and laminar flows show that the pressure drop in the bubble column is always greater; the smaller loss in the pipes suggests, therefore, that they do not represent a restriction for the flow. Indeed, the pressure drop in the pipes is always at least a factor of three smaller than in the bubble column. The connection to the bottom tanks consists of six additional gate valves fitted to the pipe outlets, in turn connected to flexible couplings [Fig. 3(c)] to accommodate tilting of the kit. The gate valves are used to control the lower boundary condition for the experiments: zero flux (closed valves) or concurrent flow (open values). Each valve is operated via a double-acting air-actuated cylinder, and all the cylinders are controlled simultaneously. The valves also provide for rapid shut-off of the flow as a safety feature.

The bottom tank receives the liquid from the header tank during recirculating flow. The tank contains a baffle system to ensure even flow over the entire length of the tank. The liquid and bubbles flow upward into the main bubble column via a 3 cm by a 3 m aperture. The tank also hosts the gas injection system (i.e., the bubbler).

Three glass panels on the front of the tank allow observation, and the tank is illuminated externally by a 3-m-long LED strip.

C. Injection system

Bubble generation is achieved by direct injection of compressed air through 17 individually controlled orifices. The injection system is a critical component of the apparatus: the way in which the bubbles are formed and the fluxes introduced into the system will affect all the resulting flow processes. Preliminary experiments showed how bubbling regimes in in-line multi-orifice sharing a common gas chamber are characterized by varying degrees of bubbling synchronicity among the orifices. It is rare to reach full synchronicity among the orifices, in most of the observed bubbling regimes, several orifices are inactive, and the active ones are often not synchronized (Capponi and Llewellin, 2019). A more controllable, stable, and reproducible gas injection system is required; this was achieved by controlling gas flow to each orifice manually. Each orifice is isolated from its neighbors and connected to its own gas chamber. The chamber dimensions and orifice diameter ranges were selected based on previous experimental investigations, which showed that bubbles may form under three different flow conditions: constant-flow conditions, where gas flux from the chamber to the forming bubble is constant; constant-pressure conditions, where pressure in the chamber is constant; and intermediate conditions, where both flux into the forming bubble and the chamber pressure vary (Kumar and Kuloor, 1970; Tsuge and Hibino, 1983). The flow condition controls bubble formation dynamics, frequency, and volume (e.g., Kumar and Kuloor, 1970; Tsuge and Hibino, 1983; Capponi and Llewellin, 2019). To discriminate the different bubbling regimes depending on the orifice diameter, we used the dimensionless capacitance number (Tsuge and Hibino, 1983),

$$N_c = \frac{4V_M\gamma g(\rho_l - \rho_g)}{\pi D_o^2 \rho_g c^2}, \tag{5}$$

where γ is the gas specific heat ratio, ρ_l and ρ_g are the density of the liquid and the gas, respectively, V_M is the volume of the gas chamber, D_0 is the orifice diameter, and c is the sound speed in the gas. For constant-flow conditions, $N_c < 1$; for intermediate conditions, $1 < N_c < 9$; and for constant-pressure conditions, $N_c > 9$ (Fig. 5). For the selected volume of each module of the bubbler, the range of available orifice diameters, and properties of the end-member liquids in use, the capacitance number for our experiments spans the range $0.8 < N_c < 28$; consequently, we can control the bubbling regime, depending on the experimental conditions (Fig. 5).

The bubbler consists of a 3-m-long stainless-steel U-section support, into which the 17 stainless-steel modules slot (Fig. 6). The identical modules have dimensions, 15 × 5 × 5 cm and wall thickness 3 mm, with a 5 mm threaded hole on top and an 8 mm threaded hole on the back. The modules are kept in place by pneumatic elbow bulkheads screwed on one side through the U-section into the 8-mm hole. The bulkheads are then connected through push-in fittings to air hoses of 8 mm diameter, all of equal length, which connect to the main compressed air line. On the top of the modules, stainless-steel non-return valves screw to the 5 mm threaded hole. A brass bolt with a precisely drilled orifice through its long axis mounts on the outlet of the valve (Fig. 6). These bolts are changeable, and a dedicated pillar drill has been prepared in the laboratory to use for drilling

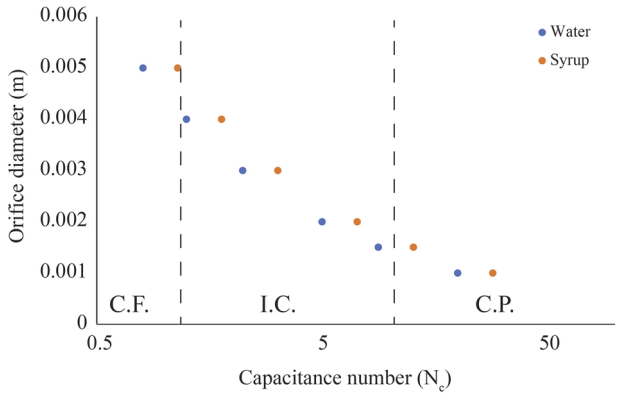

FIG. 5. Flow regime in which bubbles form for different orifice diameters in the range of 0.001–0.005 m, as a function of the dimensionless capacitance number, N_c. For $N_c < 1$: constant-flow conditions (C.F.); $1 < N_c < 9$: intermediate conditions (I.C.); $N_c > 9$: constant-pressure conditions (C.P.).

orifices of different diameter, up to 5 mm. Using non-return valves allows the gas to flow out while stopping liquid weeping through the orifices, which may potentially affect the bubble formation (e.g., Kulkarni and Joshi, 2005).

The modules are fed from the laboratory compressed air line system through a Camozzi pressure regulator (pressure range 0–10 bar) to minimize pressure fluctuations. The regulator connects to a manifold that branches into 17 sub-lines, one for each module. Each line connects, via a manually operated air switch, to either a 0–10 l/min (SMC PFM710S) or a 2–100 l/min (SMC PFM711S) flow switch, allowing quick selection of the desired flow rate range for each module of the bubbler. The flow switches have an integrated display to allow instant visualization of the flow rate, and an integrated needle valve for real-time precision adjustment of the flow.

The entire bubbler is held in place by two threaded stainless-steel rods, hanging from the top of the tank. The rods are long enough so that the bubbler can be positioned at any height between the base and the top of the bottom tank, either directly below the experimental slot or offset by 10 cm toward the front of the bottom tank. At its maximum height, when below the slot, all the orifices are flush with the slot. With this system, once the bolts with the desired orifice diameter are fitted, it is possible to control each orifice individually, allowing the gas flow rate to be controlled remotely. Orifices may be turned off, allowing the number and spacing of active orifices to be changed without the need to open the bottom tank [Fig. 3(d)].

D. Tilting mechanism

The entire front section of the apparatus, comprising the bubble column and the top and bottom tanks, can tilt up to 30° toward the rear of the apparatus on eight self-cleaning Mitsubishi bearings, rated for 3 tons each. The movement is controlled by a hydraulic system that was custom-designed, manufactured, and tested by Durham Lifting Ltd., Britannia Test House, Romaldkirk Rd, Middlesbrough TS2 1HB. The system comprises two identical pairs of

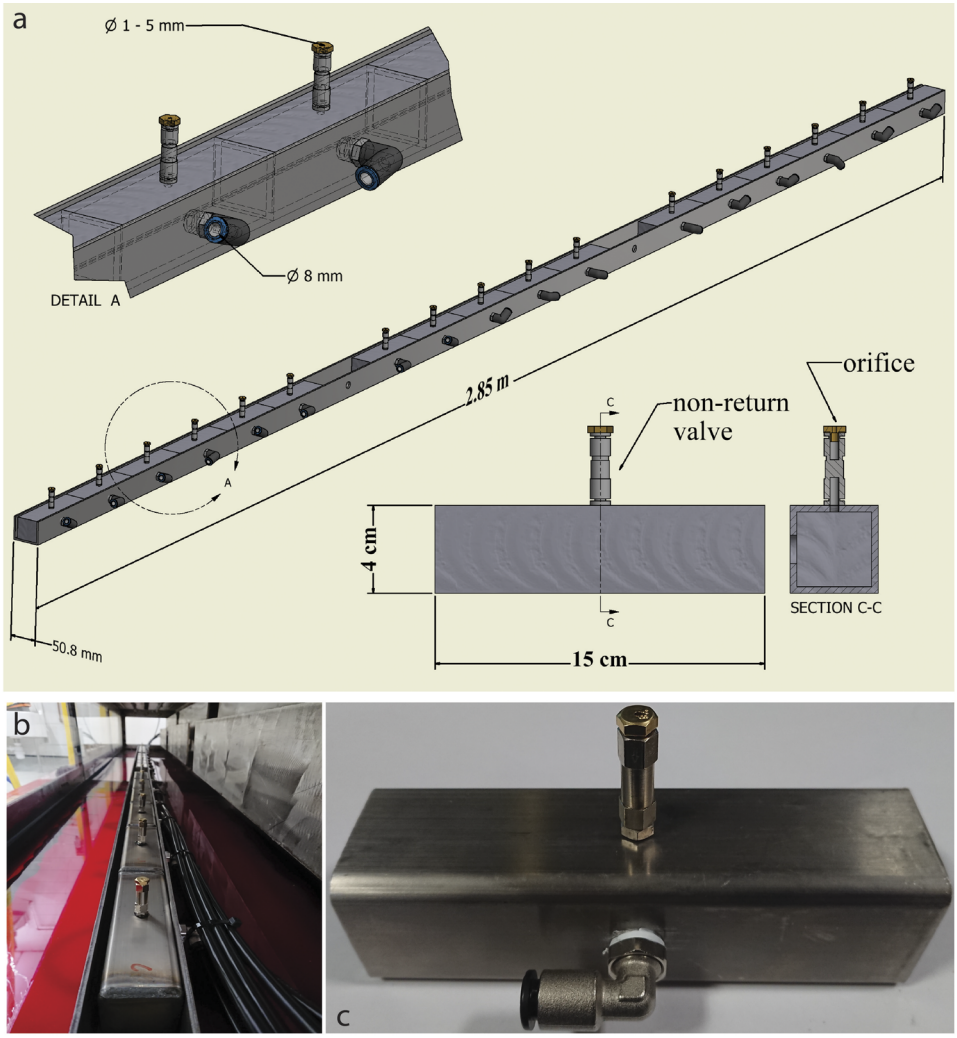

Fig. 6. (a) Technical drawing of the bubbler, showing details of the modular design. (b) The bubbler installed in the bottom tank. (c) View of one of the 17 bubble modules, comprising a small air chamber assembled with an elbow push-in fitting connector, non-return valve, and a 1 mm orifice brass bolt.

modular and extendable props, mounted on each side of the bubble column. Each pair comprises an active prop and a passive prop [Figs. 3(b) and 7(a)]. The active prop controls and actuates the tilting, while the passive prop, fitted 0.45 m below the active prop, is used as a safety control measure, to hold the front section in a fixed position at all times, except during the process of tilting. The active prop consists of a double-acting cylinder Enerpac BRD46 attached at one end to the rear glass frame and, at the other end, via either two or three extension props, to the header tank support frame. Each extension prop comprises a hollow cylinder, threaded internally, into which a cylindrical threaded rod screws. The props are designed so that 21 turns of the threaded section, which equates to 75 mm in length, accommodate an angle of 1°. The extension props, when fully extended, are 0.85 m and 0.4 m long. A long and a short prop are used for an inclination angle between 0° and 20°, while a long and two short props are used for 20°–30°. This system allows the entire front section to be tilted from 0° [i.e., vertical, Fig. 7(b)] to 30° in 1° steps [Fig. 7(c)]. The hydraulic cylinders are controlled by a hydraulic two-speed hand pump (Enerpac P84). The two passive props, one for each side, comprise the same extension props, but with the longest one 1.4 m in length when fully extended. Depending on the degree of inclination, either two or three extension props are required to secure the apparatus. To ensure the safety of operation, the safety props are removed only while operating the active props; once the hydraulic cylinders have reached their full travel, the length of the passive props is adjusted and the props are re-fitted. In front of the bubble column, as an additional safety measure, there is a fixed frame to prevent the bubble column from moving forward of vertical (Fig. 3). Two tilt sensors (Machine DRO, range 0°–360°, accuracy 0.1°) are mounted, one on each side of the bubble column, and connected via Ethernet RJ45 cables to two remote displays mounted next to the pump, to provide a continuous readout of the inclination angle.

E. Instrumentation

In addition to the flow switches and tilt sensors, which monitor in real time, respectively, variations in the gas flow rate and

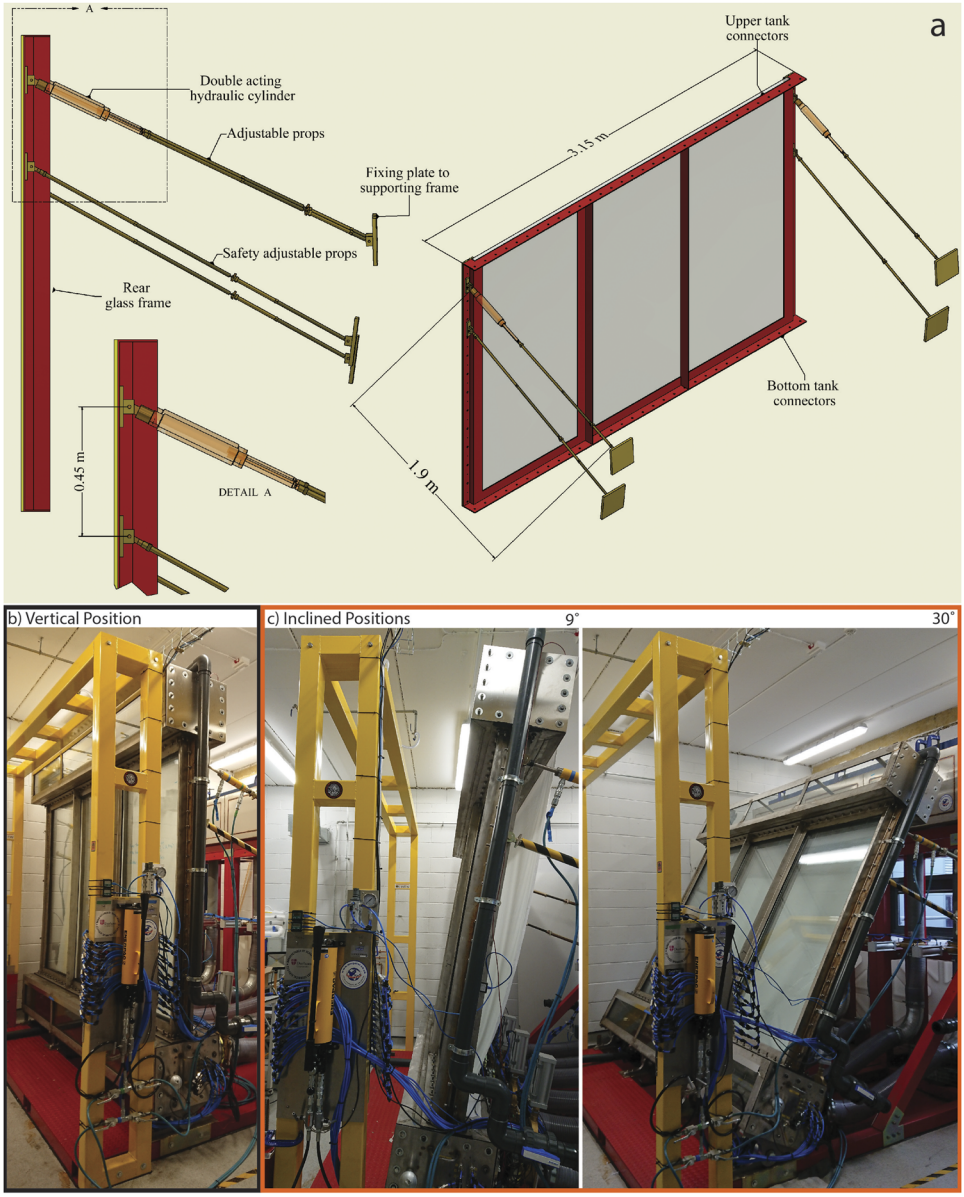

FIG. 7. (a) Technical drawing of the tilting system, connected to the rear frame of the bubble column. Note that the supporting frame, on which the other ends of the props are fixed, is not shown in the drawing. View of the experimental apparatus locked in (b) vertical position and (c) at different inclined positions (9° inclination on the left, 30° inclination on the right).

inclination angle, a suite of pressure transducers are connected to the bubbler and to the bottom tank. Pressure fluctuations within each module of the bubbler are monitored using 17 Gems gauge pressure transducers. These heavy duty transmitters cover the pressure range of 0–10 bar, have an accuracy of ±0.25%, a response time of 1 ms, and an output of 0–5 V. Two RS Pro pressure transducers are mounted on each side of the bottom tank to monitor pressure variations within the liquid at the base of the apparatus. They cover the pressure range of 0–6 bar, have an accuracy of ±0.25%, a response time of 1 ms, and an output of 4–20 mA. Temperature is monitored via three thermocouples: within the bottom tank; at the top of the fissure; and within the header tank. The thermocouples are heavy-duty PT100 PRT 4-wires probes, with 6-mm probe diameter, and temperature range of −100 °C to 450 °C. All pressure and temperature data are logged using a modular National Instruments CompactDAQ datalogger, which comprises an Ethernet 4-slot chassis cDAQ-9185 (bus bandwidth 125 Mb/s) hosting three modules; one for current (NI-9203 DAQ module, 8-channel, ±20 mA, 200 kHz/s, 16-bit analog input module), one for voltage (NI-9205, 16 differential/32 single-ended analog inputs, ±200 mV to ±10 V, 16 bit, 250 kHz/s), and one for temperature (NI-9216, eight analog inputs for PT100 RTD measurements, 0 Ω–400 Ω, 24 bit, 400 Hz/s).

Flow processes are imaged using an Emergent Vision Technologies high-speed camera HR-2000. This color camera uses a high

speed 10 GigE SFP + interface to record at 338 fps at full resolution (2048 × 1088), via a 2/3 in. CMOS sensor with a 5.5 μm square pixel. Using a 8 mm lens, from a working distance of 2.3 m and a 6 mm focal length, the camera field of view is 2.53 × 3.4 m, and hence the camera covers the entire view of the bubble column. Videos are saved as image stacks, with each frame stored in the same folder and saved in one of the most common file types for images (e.g., jpeg, bitmap, and tiff). Image frames can be opened at a later stage as a stack either for simple visual analysis or for more complex quantitative analysis. We did not develop a specific analysis technique for the image processing; however, images can be processed using established dedicated software (e.g., ImageJ or Fijy, Schindelin *et al.*, 2012) or image processing algorithms, such as PIV (e.g., Thielicke, 2014).

Both the data logger and the camera are controlled by a custom-design workstation for real time data acquisition (high-speed video and synchronized metadata), linked via high-speed networking (10 GigE), and with support for simultaneous high-speed acquisition from multiple high-speed cameras, if required. A code was designed in LabVIEW to control the data acquisition. It allows the modules installed in the data logger to be controlled individually, all together, or in groups, and directly indexes each image frame to data from the sensors.

F. Design limitations

The experimental apparatus is an idealized representation of the natural volcanic system and is not designed to capture all of its complexities. The glass panels are smooth and rigid, and hence conduit wall roughness, obstacles, elastic deformation, narrowing and widening of the dyke, and dyke sinuosity are not captured. The effects of the temperature variation on flow processes are neglected. The apparatus is not designed to reproduce magma fragmentation or the flow of gas–particle dispersion and cannot fully reproduce near-surface gas expansion effects because the upper boundary is open to the atmosphere, and cannot be held at reduced pressure. Notwithstanding these design limitations, experimental observations of development of flow regimes, bubble interactions, associated pressure changes, and flow organization patterns can be interpreted in terms of fundamental first-order fluid dynamic processes, as for the case of previous experimental investigations (e.g., Phillips *et al.*, 1995; Seyfried and Freundt, 2000; Lane *et al.*, 2001; James *et al.*, 2004, 2008; Pioli *et al.*, 2012, 2017; Del Bello *et al.*, 2015; and Capponi *et al.*, 2016; 2017)

IV. PRELIMINARY TESTS

The apparatus is designed to investigate gas–liquid organization in multiphase flows in a slot geometry. In order to test the functionality of the apparatus, we performed preliminary experiments for two different cases: (1) single bubble injection from a single emission point and (2) continuous gas supply at low and high flow rates, from three emission points. We conducted the tests in water, under stagnant conditions (no concurrent flow) and with the experimental dyke in the vertical position. A summary of experimental parameters can be found in Table III.

TABLE III. Summary of experimental parameters for test experiments.

Experimental condition	
Density ρ (kg/m^3)	1000
Viscosity μ (Pa s)	0.001
Surface tension σ (N/m)	0.07
Gravity g (m/s^2)	9.81
Conduit width D (m)	0.03
Low flow rate (l/min)	2
High flow rate (l/min)	10
Single bubble injected volume (l)	0.7
Emission orifice diameter (mm)	1
Emission point spacing (cm)	15

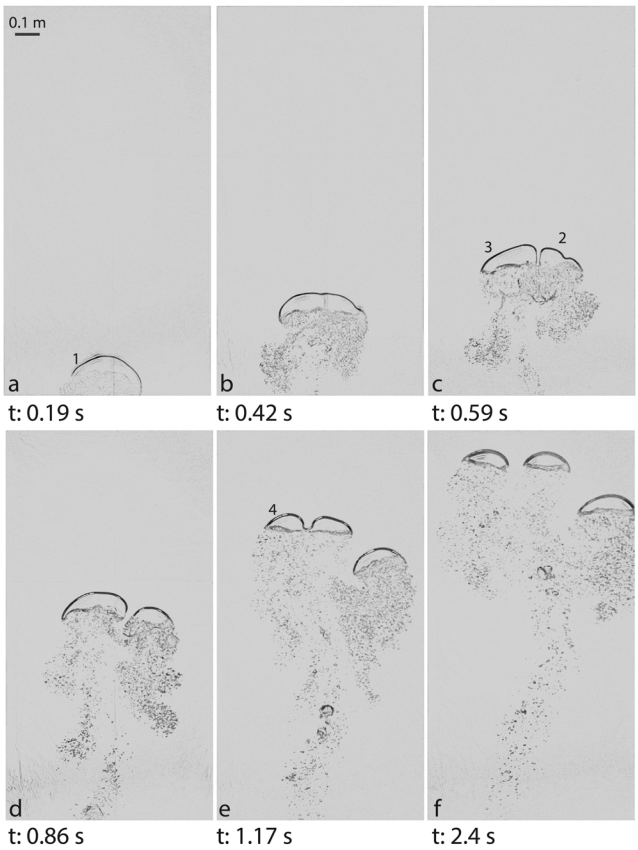

FIG. 8. Still frames at different time steps for a single gas bubble ascending in the bubble column. See text for a description of the processes occurring at each time step. Numbers in (a), (c), and (e) indicate the original parent bubble (1) and daughter bubbles (2–4) formed by instabilities that break up the bubbles. Video of the experimental run recorded at 330 fps, for the injection of 0.7 l of air from a single injection point, in water, under stagnant conditions and with the bubble column in the vertical position. Natural duration of the video is 2.5 s. Multimedia view: https://doi.org/10.1063/1.5126775.1

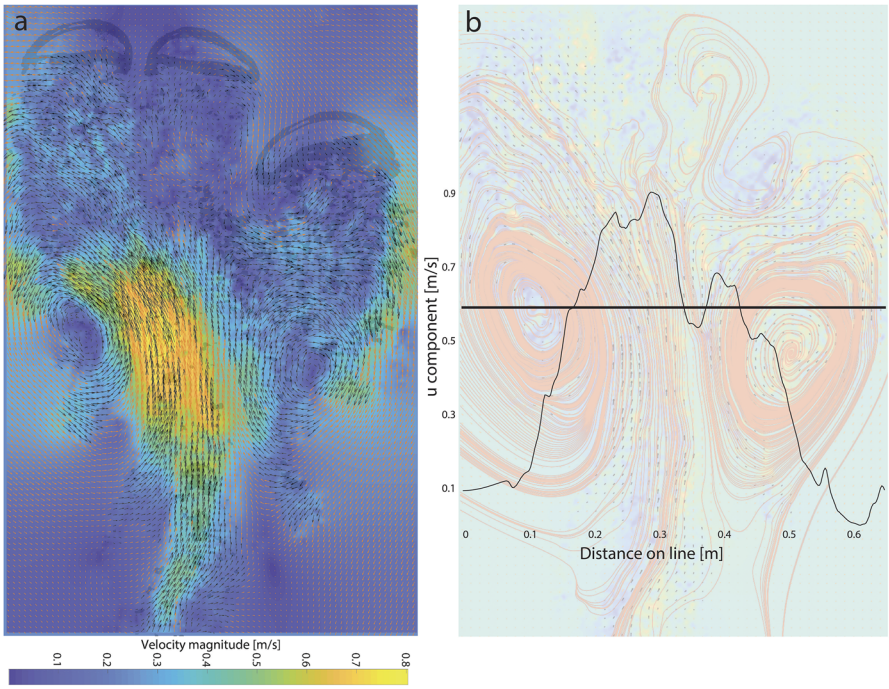

Fig. 9. (a) Particle image velocimetry measurements for the velocity field in the flow for a single gas bubble ascending in the bubble column and breaking up into three daughter bubbles; (b) streamlines highlight the main hydrodynamic features of the flow, and the velocity profile of the flow along the black horizontal line shows the rising bubble plume.

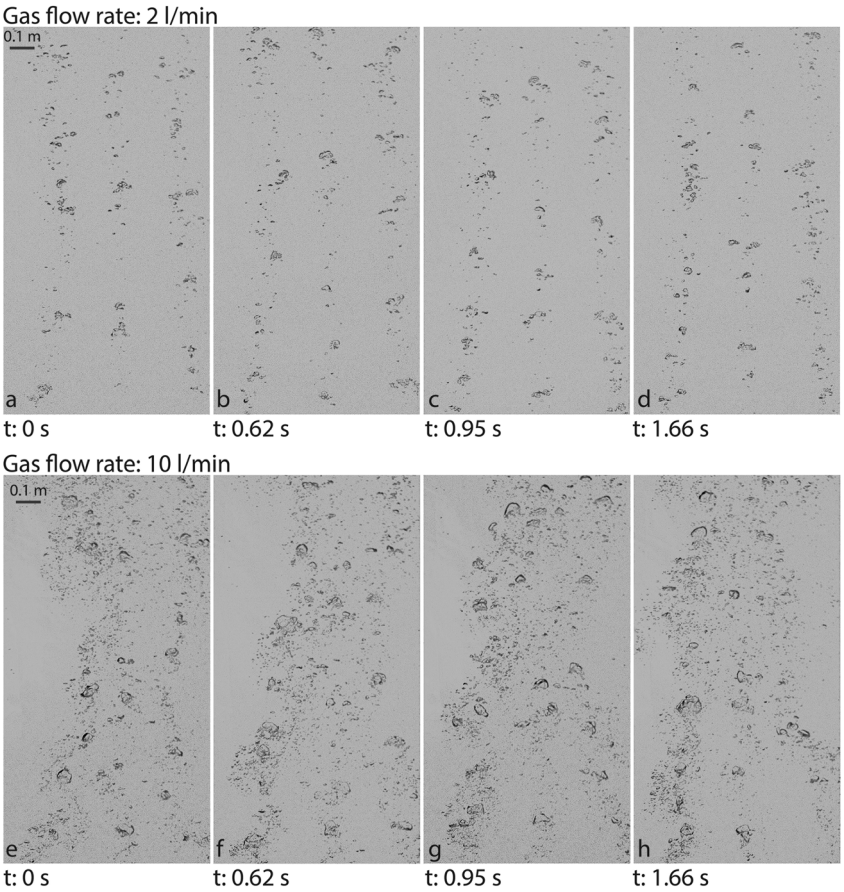

FIG. 10. Still frames of experiments with continuous gas supply from three emission points with an orifice diameter of 1 mm and spacing of 15 cm, for a gas flow rate of 2 l/min (a)–(d) and 10 l/min (e)–(h). Videos of the experimental runs were recorded at 330 fps for a continuous gas flow rate of 2 l/min (natural duration of the video is 2 s) and of 10 l/min (natural duration of the video is 3 s) through three adjacent emission points, in water, under stagnant conditions, and with the bubble column in the vertical position (Multimedia view: https://doi.org/10.1063/1.5126775.2; https://doi.org/10.1063/1.5126775.3).

A. Single bubble injection

Previous studies have shown that a gas bubble that fills the cross section of a cylindrical pipe (a Taylor bubble or "slug") is stable when the liquid ahead of the bubble is stagnant (Batchelor, 1987). For analog basaltic conduits, this has been demonstrated experimentally for diameters up to 0.25 m (e.g., James *et al.*, 2004, 2011; Pioli *et al.*, 2012; and Llewellin *et al.*, 2013) and numerically for basaltic conduits of diameter up to 10 m (e.g., James *et al.*, 2008; Chouet *et al.*, 2010). At higher values of inverse viscosity ($N_f \gtrsim 1500$), daughter bubbles are produced by turbulent "sloshing" of liquid at the tail of the bubble (e.g., Viana *et al.*, 2003; Morgado *et al.*, 2016; and Nogueira *et al.*, 2006); however, the main body of the bubble does not break up. We use the apparatus to investigate the cognate problem of the ascent of a bubble that spans the width of a slot; this scenario has not been reported in the literature for the high Eötvös number regime.

A large gas bubble is formed by injecting 0.7 l of air from the central emission point of the bubbler, flush with the base of the dyke. The gas initially rises as a single, coherent bubble that is lunate in shape, which sheds many very small satellite bubbles from its base and margins [Figs. 8(a) and 8(b) (Multimedia view)]. In sharp contrast to the Taylor bubbles that form in cylindrical pipes, the main lunate bubble is susceptible to dynamic instabilities that develop on its upper surface, and which cause it to break into two similar daughter bubbles within 0.5 s of injection [Figs. 8(c) and 8(d) (Multimedia view)]. These daughter bubbles are themselves prone to similar instabilities [Figs. 8(d) and 8(e) (Multimedia view)], and a second breakup occurs after 1 s, generating a third bubble [Fig. 8(f) (Multimedia view)]. The original parent bubble ascends at 0.83 m/s, while the daughter bubbles ascend with lower velocities (0.75 m, 0.63 m/s). In addition, each of the large bubbles is characterized by multiple smaller satellite bubbles that trail behind and ascend with them, fully entrained by the wake flow.

We can use the experimental data to extract information on flow organization and flow velocities. For this test, we used PIVLab to identify the main hydrodynamic features characterizing the flow and ImageJ and the MTrackJ plug-in to measure the velocity of the bubbles. PIVLab is a GUI-based open source Matlab tool that calculates velocities in image data and identifies flow characteristics using Particle Image Velocimetry (PIV) and several built-in MATLAB features (Thielicke, 2014; Thielicke and Stamhuis, 2014a). The ascent velocity of the bubbles was measured using the freeware software ImageJ and the MTrackJ plug-in (Abràmoff *et al.*, 2004). First, we defined the spatial scale for the images, using a calibration image for the test, so that ImageJ can automatically convert any pixel distance to centimeters. Then, we tracked for each frame the trajectory of the ascending bubble. Finally, we calculated the average velocity for the tracked trajectory over the measured frames. Figure 9 illustrates various ways in which the quantitative flow data extracted may be plotted to reveal the complex hydrodynamics associated with the ascent of a bubble in a slot. Each ascending daughter bubble forms its own circulation cell, with an open wake at its tail, which produces

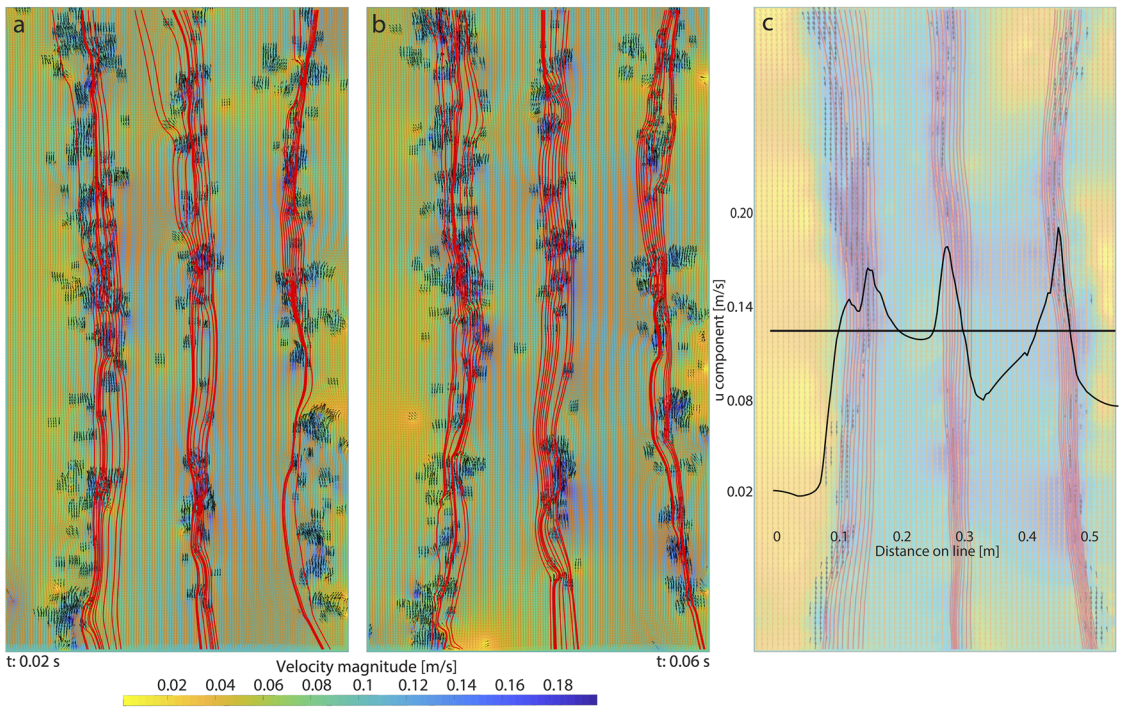

FIG. 11. Particle image velocimetry measurements for the velocity field in the flow and streamlines for three bubble plumes that form under continuous gas injection (gas flow rate: 2 l/min) from three emission points (orifice diameter: 1 mm) at (a) t: 0.02 s and (b) t: 0.06 s. (c) Streamlines highlight the main hydrodynamic features of the flow, and the velocity profile of the flow along the horizontal black line shows the rising bubble plumes.

turbulent eddies [Fig. 9(a)]. The eddies entrain the small satellite bubbles, causing them to interact, and sometimes to coalesce. Further behind the larger bubbles, where the effects of the wake have dissipated, the smaller satellite bubbles rise in a central plume, with the formation of two large gas-driven liquid circulation cells, one on either side of the plume [Fig. 9(a)]. The plume and associated circulation cells are most clearly shown by the streamlines and the flow velocity profile [Fig. 9(b)].

B. Continuous gas supply

Air was injected continuously and simultaneously from three adjacent emission points, spaced 15 cm apart, at two different gas flow rates: 2 l/min and 10 l/min.

In the first test (2 l/min), gas was injected continuously for 15 min. Small bubbles rise from each emission point, developing three distinct plumes [Figs. 10(a)–10(d) (Multimedia view)]. The bubbles share similar size, velocity, and trajectories, and the plumes show a wavy and oscillatory behavior, due to the formation of small liquid circulation cells at their sides. However, interaction among the plumes is limited, and each plume remains separated by approximately the emission point spacing during ascent. Within the plumes, bigger bubbles constantly ascend and interact with each other. Despite their interaction and the apparent collisions, these bubbles group and deform irregularly without coalescence, and group together, rising as rafts of bubbles of similar size, and sharing similar deformation patterns [Figs. 10(a)–10(d) (Multimedia view)]. As long as the flow rate is held constant, this flow pattern remains stable and is maintained throughout the entire duration of the experiment.

In the second test (10 l/min), the increase in gas flow rate leads to a higher concentration of small bubbles within each plume, increased interaction, and coalescence among the bubbles throughout their ascent, and higher bubble ascent velocity. The plumes are formed mainly of larger bubbles that ascend singly or as raft, with smaller bubbles dispersed within the plumes [Figs. 10(e)–10(h) (Multimedia view)]. The three plumes interact with one other; in particular, the outer plumes oscillate strongly, converging alternately toward the central one, coalescing and splitting cyclically [Figs. 10(e)–10(h) (Multimedia view)]. During the entire duration of the experiment, the bubble plume generated by all the emission points continually migrates from one side of the fissure [Figs. 10(e) and 10(f) (Multimedia view)] to the other [Figs. 10(g) and 10(h) (Multimedia view)], due to the large-scale liquid circulation cells developing one either side of the bubble plume [Fig. 10 (Multimedia view)].

By applying PIV (Thielicke, 2014; Thielicke and Stamhuis, 2014b) to these two cases, we can clearly observe how the flow evolves differently depending on the gas flow rate. For the 2 l/min test, PIV analysis shows that the three bubble plumes remain distinct [Figs. 11(a) and 11(b)] and have similar velocity profiles [Fig. 11(c)] with the plumes ascending more rapidly than the liquid that separates them. In contrast, the 10 l/min test shows strong interaction among the plumes, evolving cyclically over time [Figs. 12(a) and 12(c)]. The velocity profile of two merged plumes shows a significant increase in velocity, compared to the velocity of an individual plume [Fig. 12(c)], and that three merged plumes ascend more rapidly still [Fig. 12(d)].

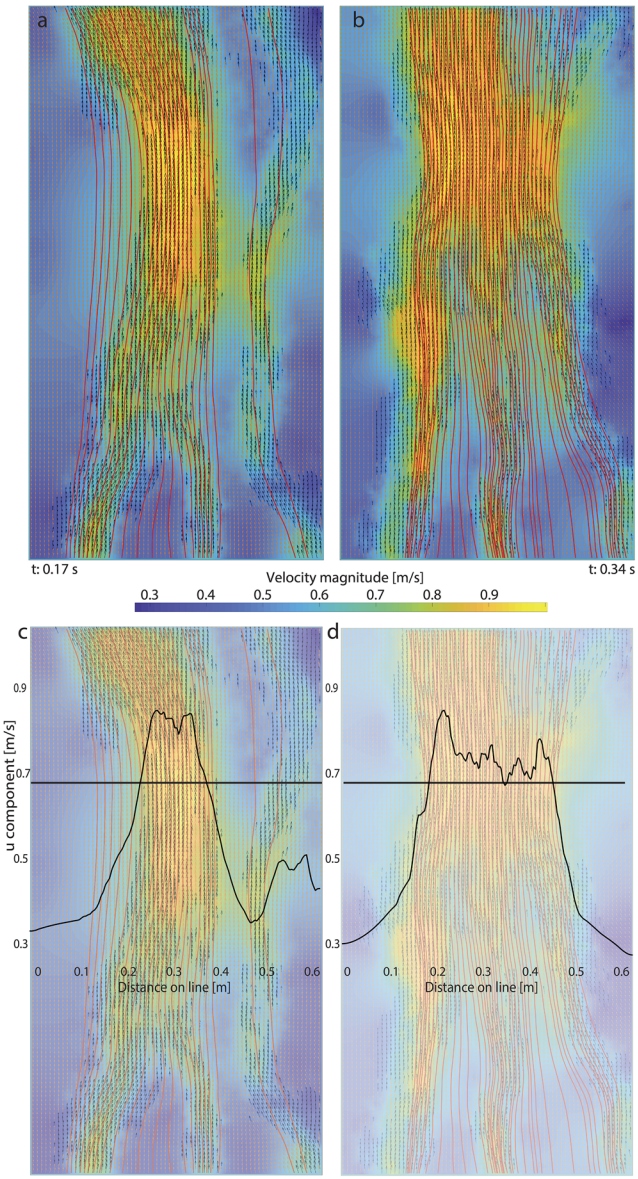

FIG. 12. Particle image velocimetry measurements for the velocity field in the flow and streamlines for three bubble plumes that form under continuous gas injection (gas flow rate: 10 l/min) from three emission points (orifice diameter: 1 mm). Note how the outer right plume (a) splits and (b) merges over time with the other two plumes. (c) and (d) Streamlines highlight the main hydrodynamic features of the flow and velocity profiles along the black horizontal lines show the structure of the flow at (c) t: 0.17 s and (d) t: 0.34 s.

V. CONCLUSIONS

We present a unique, new experimental apparatus, designed to investigate the fluid dynamic processes associated with bubbly flows in slot geometries. Specifically, the apparatus has been geometrically and dynamically scaled to model the behavior of multiphase magma in natural basaltic volcanic systems—the geometry of the apparatus

mimics the slot-like geometry of the dykes that feed most basaltic eruptions. The apparatus is designed to allow the user to explore the effect of slot inclination, variable liquid and gas fluxes, different bottom boundary conditions, and different liquid rheology on the gas–liquid flow patterns. The gas injection system is modular and flexible such that the user can vary the number, spacing, and diameter of the gas emission points. The bubble column has glass walls, allowing flow patterns to be observed and recorded directly, and the apparatus is instrumented to record pressure and temperature throughout the system. Future experiments will help to identify the processes leading to the development of different gas and liquid flow patterns, and to quantify the spatial and temporal evolution of the flows. Thus, the results will provide key constraints and input data for the development of numerical models of flow in volcanic conduits. In addition to the specific volcanological application, the apparatus will contribute to increasing our knowledge of fundamental processes associated with the formation and ascent of bubbles and bubble plumes in a narrow slot geometry.

ACKNOWLEDGMENTS

A.C. and E.W.L. gratefully acknowledge the support from Grant No. NSFGEO-NERC NE/N018443/1, *Quantifying disequilibrium processes in basaltic volcanism*. The authors are grateful to the Mechanical Workshop of the Physics Department, Durham University, for their support in assembling the experimental apparatus. We thank James Dyson for his invaluable support in setting up the new Volcanological Fluid Dynamics Laboratory. A.C. and A.C.C. are also grateful to Antonia Hofmann, Fadul Dawood, James Dyson, and Ian Chaplin for assistance during several assembly procedures.

REFERENCES

Abràmoff, M. D., Magalhães, P. J., and Ram, S. J., "Image processing with ImageJ," Biophotonics Int. **11**(7), 36–42 (2004).

Batchelor, G. K., "The stability of a large gas bubble rising through liquid," J. Fluid Mech. **184**, 399–422 (1987).

Beckett, F. M. *et al.*, "Conduit convection driving persistent degassing at basaltic volcanoes," J. Volcanol. Geotherm. Res. **283**, 19–35 (2014).

Bruce, P. M. and Huppert, H. E., "Thermal control of basaltic fissure eruptions," Nature **342**(6250), 665 (1989).

Capponi, A., James, M. R., and Lane, S. J., "Gas slug ascent in a stratified magma: Implications of flow organisation and instability for Strombolian eruption dynamics," Earth Planet. Sci. Lett. **435**, 159 (2016).

Capponi, A., Lane, S. J., and James, M. R., "The implications of gas slug ascent in a stratified magma for acoustic and ground deformation source mechanisms in Strombolian eruptions," Earth Planet. Sci. Lett. **468**, 101–111 (2017).

Capponi, A. and Llewellin, E. W., "Experimental observations of bubbling regimes at in-line multi-orifice bubblers," Int. J. Multiphase Flow **114**, 66 (2019).

Chouet, B. A., Dawson, P. B., James, M. R., and Lane, S. J., "Seismic source mechanism of degassing bursts at Kilauea Volcano, Hawaii: Results from waveform inversion in the 10–50 s band," J. Geophys. Res. **115**, B09311, https://doi.org/10.1029/2009JB006661 (2010).

Del Bello, E., Lane, S. J., James, M. R., Llewellin, E. W., Taddeucci, J., Scarlato, P., and Capponi, A., "Viscous plugging can enhance and modulate explosivity of strombolian eruptions," Earth Planet. Sci. Lett. **423**, 210–218 (2015).

Gonnermann, H. and Taisne, B., "Magma transport in dikes," in *The Encyclopedia of Volcanoes* (Academic Press, 2015), pp. 215–224.

Gurioli, L., Colò, L., Bollasina, A. J., Harris, A. J. L., Whittington, A., and Ripepe, M., "Dynamics of strombolian explosions: Inferences from field and laboratory studies of erupted bombs from Stromboli volcano," J. Geophys. Res. **119**, 319–345, https://doi.org/10.1002/2013JB010355 (2014).

Houghton, B. F. and Gonnermann, H. M., "Basaltic explosive volcanism: Constraints from deposits and models," Geochemistry **68**(2), 117–140 (2008).

James, M. R., Lane, S. J., Chouet, B., and Gilbert, J. S., "Pressure changes associated with the ascent and bursting of gas slugs in liquid-filled vertical and inclined conduits," J. Volcanol. Geotherm. Res. **129**, 61–82 (2004).

James, M. R., Lane, S. J., and Chouet, B. A., "Gas slug ascent through changes in conduit diameter: Laboratory insights into a volcano-seismic source process in low-viscosity magmas," J. Geophys. Res. **111**(B5), B05201, https://doi.org/10.1029/2005JB003718 (2006).

James, M. R., Lane, S. J., and Corder, S. B., "Modelling the rapid near-surface expansion of gas slugs in low viscosity magmas," Geol. Soc., London, Spec. Publ. **307**(1), 147–167 (2008).

James, M. R., Llewellin, E. W., and Lane, S. J., "Comment on "It takes three to tango: 2. Bubble dynamics in basaltic volcanoes and ramifications for modeling normal strombolian activity" edited by J. Suckale, B. H. Hager, L. T. Elkins-Tanton, and J.-C. Nave," J. Geophys. Res. **116**, B06207, https://doi.org/10.1029/2010JB008167 (2011).

Jaupart, C. and Vergniolle, S., "The generation and collapse of a foam layer at the roof of a basaltic magma chamber," J. Fluid Mech. **203**, 347–380 (1989).

Jones, T. J., Llewellin, E. W., Houghton, B. F., Brown, R. J., and Vye-Brown, C., "Proximal lava drainage controls on basaltic fissure eruption dynamics," Bull. Volcanol. **79**(11), 81 (2017).

Kervyn, M., Ernst, G. G. J., van Wyk de Vries, B., Mathieu, L., and Jacobs, P., "Volcano load control on dyke propagation and vent distribution: Insights from analogue modeling," J. Geophys. Res. **114**(B3), B03401, https://doi.org/10.1029/2008jb005653 (2009).

Kobayashi, T., Namiki, A., and Sumita, I., "Excitation of airwaves caused by bubble bursting in a cylindrical conduit: Experiments and a model," J. Geophys. Res. **115**, B10201, https://doi.org/10.1029/2009JB006828 (2010).

Kulkarni, A. A. and Joshi, J. B., "Bubble formation and bubble rise velocity in gas–liquid systems: A review," Ind. Eng. Chem. Res. **44**(16), 5873–5931 (2005).

Kumar, R. and Kuloor, N. K., "The formation of bubbles and drops," in *Advances in Chemical Engineering* (Academic Press, 1970), Vol. 8, pp. 255–368.

Lane, S. J., Chouet, B. A., Phillips, J. C., Dawson, P., Ryan, G. A., and Hurst, E., "Experimental observations of pressure oscillations and flow regimes in an analogue volcanic system," J. Geophys. Res. **106**(B4), 6461–6476, https://doi.org/10.1029/2000jb900376 (2001).

Lane, S. J., James, M. R., and Corder, S. B., "Volcano infrasonic signals and magma degassing: First-order experimental insights and application to Stromboli," Earth Planet. Sci. Lett. **377-378**, 169–179 (2013).

Lister, J. R. and Kerr, R. C., "Fluid-mechanical models of crack propagation and their application to magma transport in dykes," J. Geophys. Res. **96**(B6), 10049–10077, https://doi.org/10.1029/91jb00600 (1991).

Llewellin, E., Del Bello, E., Lane, S., Capponi, A., Mathias, S., and Taddeucci, J., "Cyclicity in slug-driven basaltic eruptions: Insights from large-scale analogue experiments," in *EGU General Assembly Conference Abstracts* (Geophysical Research Abstracts, EGU, 2013), Vol. 15.

Llewellin, E. W., Del Bello, E., Taddeucci, J., Scarlato, P., and Lane, S. J., "The thickness of the falling film of liquid around a Taylor bubble," Proc. R. Soc. Math. Phys. Eng. Sci. **468**(2140), 1041–1064 (2012).

Llewellin, E. W., Mader, H. M., and Wilson, S. D. R., "The rheology of a bubbly liquid," Proc. R. Soc. A **458**, 987–1016 (2002).

Mader, H. M., Llewellin, E. W., and Mueller, S. P., "The rheology of two-phase magmas: A review and analysis," J. Volcanol. Geotherm. Res. **257**, 135–158 (2013).

Mastin, L. G., Robert, L. C., Carl, T., Jacob, L., and Melvin, B., "What makes hydromagmatic eruptions violent? Some insights from the Keanakāko'i Ash, Kīlauea Volcano, Hawai'i," J. Volcanol. Geotherm. Res. **137**, 15–31 (2004).

Métrich, N., Bertagnini, A., Landi, P., and Rosi, M., "Crystallization driven by decompression and water loss at Stromboli volcano (Aeolian Islands, Italy)," J. Petrol. **42**(8), 1471–1490 (2001).

Morgado, A. O., Miranda, J. M., Araújo, J. D. P., and Campos, J. B. L. M., "Review on vertical gas–liquid slug flow," Int. J. Multiphase Flow **85**, 348–368 (2016).

Mueller, S., Llewellin, E. W., and Mader, H. M., "The effect of particle shape on suspension viscosity and implications for magmatic flows," Geophys. Res. Lett. **38**(13), L13316, https://doi.org/10.1029/2011gl047167 (2011).

Murase, T. and McBirney, A. R., "Properties of some common igneous rocks and their melts at high temperatures," Geol. Soc. Am. Bull. **84**(11), 3563–3592 (1973).

Nogueira, S., Riethmuller, M. L., Campos, J. B. L. M., and Pinto, A. M. F. R., "Flow patterns in the wake of a Taylor bubble rising through vertical columns of stagnant and flowing Newtonian liquids: An experimental study," Chem. Eng. Sci. **61**(22), 7199–7212 (2006).

Orr, T. R., Poland, M. P., Patrick, M. R., Thelen, W. A., Sutton, A. J., Elias, T., Thornber, C. R., Parcheta, C., and Wooten, K. M., "Kilauea's 5–9 March 2011 Kamoamoa fissure eruption and its relation to 30+ years of activity from Pu'u "O"o," in *Hawaiian Volcanoes: From Source to Surface, American Geophysical Union Geophysical Monograph*, edited by Carey, R., Poland, M., Cayol, V., and Weis, D. (John Wiley & Sons, 2015), Vol. 208.

Palma, J. L., Blake, S., and Calder, E. S., "Constraints on the rates of degassing and convection in basaltic open-vent volcanoes," Geochem. Geophys. Geosyst. **12**, Q11006, https://doi.org/10.1029/2011GC003715 (2011).

Parcheta, C., Fagents, S., Swanson, D. A., Houghton, B. F., and Ericksen, T., "Hawaiian fissure fountains," in *Hawaiian Volcanoes*, edited by Carey, R., Cayol, V., Poland, M., and Weis, D. (Wiley, 2015), Vol. 208, pp. 369–391.

Parcheta, C. E., Houghton, B. F., and Swanson, D. A., Bull. Volcanol. **74**, 1729 (2012).

Parfitt, E. A., "A discussion of the mechanisms of explosive basaltic eruptions," J. Volcanol. Geotherm. Res. **134**(1-2), 77–107 (2004).

Parfitt, E. A., Wilson, L., and Neal, C. A., Bull. Volcanol. **57**, 440 (1995).

Phillips, J. C., Lane, S. J., Lejeune, A.-M., and Hilton, M., "Gum rosin-acetone system as an analogue to the degassing behaviour of hydrated magmas," Bull. Volcanol. **57**(4), 263–268 (1995).

Pinel, V. and Jaupart, C., "The effect of edifice load on magma ascent beneath a volcano," Philos. Trans. R. Soc. London, Ser. A **358**(1770), 1515–1532 (2000).

Pioli, L., Azzopardi, B. J., Bonadonna, C., Brunet, M., and Kurokawa, A. K., "Outgassing and eruption of basaltic magmas: The effect of conduit geometry," Geology **45**(8), 759–762 (2017).

Pioli, L., Bonadonna, C., Azzopardi, B. J., Phillips, J. C., and Ripepe, M., "Experimental constraints on the outgassing dynamics of basaltic magmas," J. Geophys. Res. **117**, B03204, https://doi.org/10.1029/2011JB008392 (2012).

Reynolds, H. I., Gudmundsson, M. T., Högnadóttir, T., Magnússon, E., and Pálsson, F., "Subglacial volcanic activity above a lateral dyke path during the 2014–2015 Bárdarbunga-Holuhraun rifting episode, Iceland," Bull. Volcanol. **79**(6), 38 (2017).

Rubin, A. M., "Propagation of magma-filled cracks," Annu. Rev. Earth Planet. Sci. **23**(1), 287–336 (1995).

Schindelin, J., Arganda-Carreras, I., Frise, E., Kaynig, V., Longair, M., Pietzsch, T., Preibisch, S., Rueden, C., Saalfeld, S., Schmid, B., Tinevez, J.-Y., White, D. J., Hartenstein, V., Eliceiri, K., Tomancak, P., and Cardona, A., "Fiji: An open-source platform for biological-image analysis," Nat. Methods **9**(7), 676–682 (2012).

Seyfried, R. and Freundt, A., "Experiments on conduit flow and eruption behaviour of basaltic volcanic eruptions," J. Geophys. Res. **105**(B10), 727–740, https://doi.org/10.1029/2000JB900096 (2000).

Shaw, H. R., "Rheology of basalt in the melting range," J. Petrol. **10**, 510–535 (1969).

Spina, L., Cimarelli, C., Scheu, B., Di Genova, D., and Dingwell, D. B., "On the slow decompressive response of volatile-and crystal-bearing magmas: An analogue experimental investigation," Earth Planet. Sci. Lett. **433**, 44–53 (2016).

Stevenson, D. S. and Blake, S., "Modelling the dynamics and thermodynamics of volcanic degassing," Bull. Volcanol. **60**(4), 307–317 (1998).

Swanson, D. A., Duffield, W. A., Jackson, D. B., and Peterson, D. W., "Chronological narrative of the 1969–1971 Mauna Ulu eruption of Kilauea Volcano, Hawaii," US Geological Survey Professional Paper No. 1056, 1979.

Thielicke, W., "The flapping flight of birds: Analysis and application," Ph.D. thesis, Rijksuniversiteit Groningen, 2014, http://irs.ub.rug.nl/ppn/382783069.

Thielicke, W. and Stamhuis, E. J., "PIVlab: Towards user-friendly, affordable and accurate digital particle image velocimetry in MATLAB," J. Open Res. Software **2**(1), e30 (2014a).

Thielicke, W. and Stamhuis, E. J., "PIVlab: Time-resolved Digital Particle Image Velocimetry Tool for MATLAB" (2014b), https://doi.org/10.6084/m9.figshare.1092508.

Thorarinsson, S., Steinthórsson, S., Einarsson, T., Kristmannsdóttir, H., and Oskarsson, N., "The eruption on Heimaey, Iceland," Nature **241**, 372–375 (1973).

Tibaldi, A., Bonali, F. L., and Corazzato, C., "The diverging volcanic rift system," Tectonophysics **611**, 94–113 (2014).

Tsuge, H. and Hibino, S. I., "Bubble formation from an orifice submerged in liquids," Chem. Eng. Commun. **22**(1-2), 63–79 (1983).

Valentine, G. A. and Gregg, T. K. P., "Continental basaltic volcanoes—Processes and problems," J. Volcanol. Geotherm. Res. **177**(4), 857–873 (2008).

Valentine, G. A., Krier, D., Perry, F. V., and Heiken, G., "Scoria cone construction mechanisms, Lathrop Wells Volcano, Southern Nevada, USA," Geology **33**(8), 629–632 (2005).

Valentine, G. A. and Perry, F. V., "Decreasing magmatic footprints of individual volcanoes in a waning basaltic field," Geophys. Res. Lett. **33**(14), L14305, https://doi.org/10.1029/2006gl026743 (2006).

Vergniolle, S., "Bubble size distribution in magma chambers and dynamics of basaltic eruptions," Earth Planet. Sci. Lett. **140**(1), 269–279 (1996).

Vergniolle, S., "Modelling two-phase flow in a volcano," in *Proceedings of the 13th Australian Fluid Mechanics Conference, Aristoc. Offset* (Monash University, Melbourne, 1998), pp. 647–650.

Vergniolle, S. and Gaudemer, Y., "From reservoirs and conduits to the surface," in *Hawaiian Volcanis*, American Geophysical Union Monograph, edited by Carey, R., Cayol, V., Poland, M., and Weis, D. (Wiley, 2015), Vol. 208, pp. 289–322.

Vergniolle, S. and Jaupart, C., "Separated two-phase flow and basaltic eruptions," J. Geophys. Res. **91**(B12), 12842–12860, https://doi.org/10.1029/jb091ib12p12842 (1986).

Viana, F., Pardo, R., Yánez, R., Trallero, J. L., and Joseph, D. D., "Universal correlation for the rise velocity of long gas bubbles in round pipes," J. Fluid Mech. **494**, 379–398 (2003).

Wallis, G. B., *One-Dimensional Two-Phase Flow* (McGraw-Hill, New York, 1969).

Wilson, L., Parfitt, E. A., and Head, J. W., "Explosive volcanic eruptions—VIII. The role of magma recycling in controlling the behaviour of Hawaiian-style lava fountains," Geophys. J. Int. **121**, 215–225 (1995).